Celestial Mechanics and Dynamical Astronomy (2018) 130:60
https://doi.org/10.1007/s10569-018-9852-6

ORIGINAL ARTICLE

Parallel initial orbit determination using angles-only observation pairs

Paul W. Schumacher Jr.[1] · John A. Gaebler[2] · Christopher W. T. Roscoe[3] · Matthew P. Wilkins[3] · Penina Axelrad[2]

Received: 17 March 2018 / Revised: 10 August 2018 / Accepted: 20 August 2018 /
Published online: 12 September 2018

Abstract
We propose a type of admissible-region analysis for track initiation in multi-satellite problems when angles are the primary observable. Pairs of optical observations are used to calculate candidate orbits via a Lambert solver by hypothesizing range values. The method is attractive because it allows multiple levels of parallelization of the track-initiation process. Orbital element partitions are introduced to divide the admissible region into smaller search spaces to be processed on individual computer nodes. For a specified rectangular partition in the space of orbital elements, constraints are developed to bound the values of range that will lead to initial orbit hypotheses (data association hypotheses) associated with that partition. These bounds allow us to parallelize the generation of candidate orbits, because each element-space partition can be handled independently of the others. Several constraints are developed and shown to limit the range pair hypotheses effectively to the constrained admissible region based on the orbital element partitions. Examples are provided to highlight the topology of the proposed constraints.

Keywords Track initiation · Constrained admissible region · Optical surveillance · Space situational awareness · Angles only · Initial orbit determination

✉ John A. Gaebler
gaebler@colorado.edu

Paul W. Schumacher Jr.
paul.schumacher@us.af.mil

Christopher W. T. Roscoe
croscoe@applieddefense.com

Matthew P. Wilkins
mwilkins@applieddefense.com

Penina Axelrad
penina.axelrad@colorado.edu

[1] Air Force Research Laboratory, Directed Energy Directorate, Space Surveillance Systems Branch, Dayton, Kihei, HI, USA

[2] Smead Aerospace Engineering Sciences, University of Colorado Boulder, Boulder, CO, USA

[3] Applied Defense Solutions, Columbia, MD, USA

1 Introduction

The advent of high-sensitivity, high-capacity optical sensors for space surveillance presents us with interesting and challenging tracking problems. Accounting for the origin of every detection made by such systems is generally agreed to belong to the "most difficult" category of tracking problems. Especially in the early phases of the tracking scenario, when a catalog of space objects is being compiled or when many new objects appear in space because of an on-orbit explosion or collision, one faces a combinatorially large number of data association hypotheses to evaluate. The number of hypotheses is reduced to a more feasible number if observations close together in time can, with high confidence, be associated by the sensor into extended tracks on single objects. Most current space surveillance techniques are predicated on the sensor system's ability to form such tracks reliably. However, the required operational tempo of space surveillance, the very large number of objects in Earth orbit and the difficulties of detecting dim, fast-moving objects at long ranges mean that individual sensor track reports are often inadequate for computing initial orbit hypotheses.

In fact, this situation can occur with optical sensors even when the probability of detection is high. For example, the arc of orbit that has been observed may be too short or may have been sampled too sparsely to allow well-conditioned, usable orbit estimates from single tracks. In that case, one has no choice but to solve a data association problem involving an unknown number of objects and many widely spaced observations of uncertain origin. In the present analysis, we are motivated by this more difficult aspect of the satellite cataloging problem.

The primary goal of this work is to capture all new orbits represented in a large set of observations in a manner that leverages the computational efficiency of modern computers. The proposed method will create a large number of candidate orbits. However, the parallelizable nature of the method helps to manage the processing time. A motivating factor is the need for methods that can keep up with incoming data. The sensor network is continually expanding, and the current system already has a high throughput of observations. Considering modern multi-target estimation methods (Jones et al. 2016; Vo et al. 2017) under development, the proposed method can be included as a birth-model in the estimation scheme to handle uncorrelated observations.

In particular, consider the angles-only case, in which angle-rate values are not available or are too inaccurate for reliable use. Assume that we have a pair of line-of-sight unit vectors $\bar{u}_1$ and $\bar{u}_2$, measured at time t_1 at station position $\bar{R}_1$ and time t_2 at station position $\bar{R}_2$, respectively. The difference between the observation times $t_2 - t_1$ is the time-of-flight Δt_{TOF}. See Fig. 1 for a visualization of the geometry. Assume, without loss of generality, that $t_2 > t_1$.

We want to test the hypothesis that these two observations are associated with the same space object. To this end, attach a set of hypothetical range values, $\{\rho_{1,m}, m = 1, 2, \dots\}$ and $\{\rho_{2,n},\ n = 1, 2, \dots\}$, respectively, to each of these measured unit vectors and then generate candidate orbits by solving Lambert's problem for each of the pair-wise combinations of hypothetical orbital position vectors $\bar{r}_{1,m}$ and $\bar{r}_{2,n}$. Then each hypothetical orbit from the solution of Lambert's problem is a hypothesis that must be either confirmed or eliminated through comparisons with other observational data. The range pairs that define a feasible orbit form a region in the (ρ_1, ρ_2) plane. Given enough range hypotheses for each observed line of sight, it is guaranteed that a viable candidate orbit is generated for every object that has been observed at two or more distinct times. With a large data-set of measured line-of-sight unit vectors, we can, in principle, consider all possible pairs of observations and solve the family of Lambert problems for each pair. However, the Cartesian product of the set of range

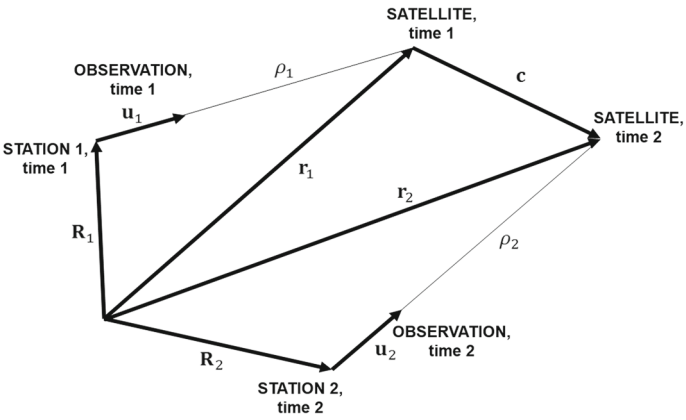

Fig. 1 Geometry of initial orbit determination problem

values for each observed line of sight with the sets of range values from every other line of sight implies a possibly prohibitive number of Lambert solutions to generate and check.

From a theoretical point of view, given N_z observations of line of sight, not necessarily close together in time, the computational load of Lambert-based methods is asymptotically proportional to N_z^2 (N_z-choose-2 combinations), because two observations per data association hypothesis are needed. The total computational complexity for generating hypothetical orbits in our approach is then $(N_z N_\rho)^2$, where N_ρ is the average number of range hypotheses considered for each observation. With traditional methods of angles-only initial orbit determination, including that of Gooding (1993, 1997) one faces a computational load that is asymptotically proportional to N_z^3 (N_z-choose-3 combinations), because three observations must be associated together to compute the range and hence the candidate orbit. The methods developed by Karimi and Mortari (2011) are more robust than traditional methods, but these also require at least three observations per association hypothesis. In fact, the approach of Karimi and Mortari works better with more observations per association hypothesis, but then one faces a computational load that scales like N_z^4, N_z^5, or even higher. In general, the computational complexity is polynomial in the number of observations, with the polynomial degree equal to the number of observations per data association hypothesis.

How should we limit the number of range hypotheses to make the total number of candidate orbits manageable while also generating candidates that are likely to correspond to real orbits of interest? If angle-rate information were available, $(\rho_1, \dot{\rho}_1)$ bounds could be imposed based on some admissible-region analysis of the type developed by numerous authors (Milani et al. 2004; Milani and Knezevic 2005; Tommei et al. 2007, 2009; Fujimoto et al. 2010; Farnocchia et al. 2010; Gronchi et al. 2010). When angles are the only observable, in a similar manner we define a region in the (ρ_1, ρ_2) plane for a pair of observations analogous to the $(\rho_1, \dot{\rho}_1)$ admissible region. We call this point set in the (ρ_1, ρ_2) plane the range–range admissible region. Section 3 discusses the definition of this range–range admissible region and provides some illustrations.

Naturally, processing every possible combination with an iterative Lambert solver could be prohibitive for serial processing of a large set of new observations. Instead, the computational burden is distributed among many computer nodes. Each node will handle a separate set of orbits by dividing the space of orbital elements into partitions. Any partition of the space of orbital elements, including the whole space itself, can be divided into smaller partitions,

Table 1 Comparison of track-initiation methods

	Classic	RR-CAR	Angle-rate CAR
Unique observations	3	2	1
Possible combinations	N_z-choose-3	N_z-choose-2	N_z
Observation types	$\bar{u}_1, \bar{u}_2, \bar{u}_3$	$\bar{u}_1, \bar{u}_2$	$\bar{u}_1, \dot{\bar{u}}_1$
Hypotheses needed	N/A	ρ_1, ρ_2	$\rho_1, \dot{\rho}_1$
Solution type	Exact	Approximate	Approximate
Solutions/candidates	1	$N_{\rho_1} \times N_{\rho_2}$	$N_\rho \times N_{\dot{\rho}}$

and each partition can be handled independently and therefore in parallel. Additional details are provided in Sect. 2. We seek to generate hypothetical range values representing only orbits that lie in a bounded region of semi-major axis a, eccentricity e, and inclination i for each partition. For the purposes of this discussion, the other orbital elements are left unconstrained. It will turn out that these three elements constrain the possible values of range in simple ways. Each partition is specified by the intervals $[a_{\min}, a_{\max}]_j$, $[e_{\min}, e_{\max}]_j$, and $[i_{\min}, i_{\max}]_j$, where j is the partition identifier. If computation time is still an issue, the partitions can be made smaller so that the overall parallel computation time is feasible, at the cost of requiring more computer nodes.

Since we are concerned with limiting the element space within each partition, we call the set of range pairs that represent an orbit defined by partition j the range–range constrained admissible region (RR-CAR), as opposed to the range–range-rate constrained admissible region explored in previous works, e.g., DeMars et al. (2012), which simply labeled it the constrained admissible region (CAR). Those prior efforts assumed that angle rates were available, and the CAR was specified for each observed line of sight independently. See Table 1 for a comparison of the methods discussed. Further discussion and comparison with the prior development of the CAR is provided in Sect. 6.

This idea for performing parallel angles-only track initiation was first introduced by Schumacher Jr. (2012a), then further developed in a series of conference papers including Schumacher et al. (2012b; 2013) and Roscoe et al. (2014). These papers presented bounds on range and range rate for single and dual observation epochs, presented examples and investigated the effects of angle-rate errors on range-rate boundaries. Other authors have sought tighter bounds on the range pair hypotheses approach developed by Schumacher et al. Fujimoto and Alfriend (2015) showed that additional hypotheses could be rejected with angle rates even if they possess large errors. Siminski et al. (2014) started with the range hypotheses approach and applied optimization techniques to find the best matching range pair. Both of these efforts were reliant on angle rates. A key feature of the approach offered in this article is that we do not need angle rates, so that we can accommodate observations from relatively simple optical sensors. A conference paper by Gaebler et al. (2017) developed the additional constraints that allowed for an effective implementation while ignoring the angle rates. The present article describes the full parallel track initiation concept and methods, presenting a complete set of constraints that can efficiently reject range hypotheses outside a given partition, thus limiting the number of costly Lambert solutions required. The overall algorithm is described in Table 2. This approach produces an effective, parallelizable track-initiation procedure.

The constraints are a set of geometric and kinematic conditions that can be applied to each range pair hypothesis. The goal of these bounds and checks is to reduce the range–

Table 2 Overall algorithm for generating candidate orbits from angles-only observations

	Steps
	Collect uncorrelated observations
1	Specify partitions on (a, e, i)
2	Enumerate combinations of uncorrelated observations
	For each partition: (in parallel)
	For each pair of observations: (serially or in parallel)
3	Compute supremum bounds for range hypotheses
4	Populate range pair hypotheses using {fine, coarse, targeted} sampling strategy
5	Reject range pair hypotheses via constraint checks
	For remaining range pair hypotheses:
6	Generate candidate orbits via Lambert solver
	Seed/birth new targets based on candidate orbits

This set of steps would ideally be a function within an overall tracking filter process. Numbered steps are directly addressed in this article

range hypothesis space as nearly as possible to the actual RR-CAR for each set of element partitions. These constraints are discussed in Sect. 4. This approach allows us to consider a manageable number of range hypotheses for each partition before generating candidate orbits via a Lambert solver.

For the purpose of developing this methodology we are assuming elliptical orbits with observations spanning a single orbital period. The limitation to a single orbital revolution is not essential to our method, as noted below in connection with the solution to Lambert's problem for each (ρ_1, ρ_2) hypothesis. We have chosen to simplify our discussion in this manner to highlight the new constraints offered here for rejecting hypotheses. Allowing multiple orbit hypotheses per range pair will not affect the use of our constraints. Our examples also ignore observation uncertainty, although nothing prevents the inclusion of such perturbations. Uncertainty in the observations does not change the logic of the method we outline, and does not change the ability to scale our method to large numbers of observations.

This report lays out the fundamentals of the methodology and introduces efficient geometric and kinematic constraints that lead to upper and lower bounds on the possible values of range for each pair of observations, given only angle data at discrete times. Several inequalities are presented that must be satisfied simultaneously, and the most restrictive superposition of the various constraints becomes the working result. These regions can be exhibited numerically, and there is plenty of opportunity for future study of the geometrical and topological properties of these regions. Section 5 provides numerical examples of the constraints for two orbital regimes. In summary, a new methodology is proposed which provides a fast and efficient means to generate candidate orbits in a large track-initiation problem.

2 Parallel track initiation

The availability of supercomputers motivates our desire to parallelize the angles-only track initiation for large cataloging problems. Classic angles-only methods, e.g., Gooding's method (1997), cannot be parallelized efficiently due to the N_z^3 scaling in the number of combinations needed and the fact that the candidate orbit solutions cannot be restricted a priori to a subset

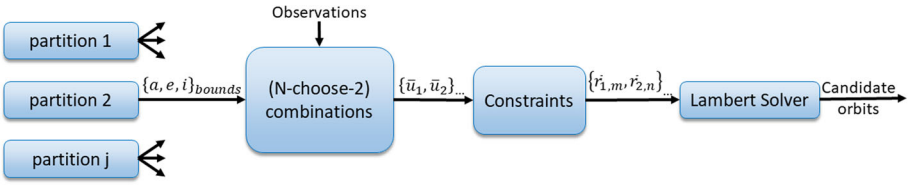

Fig. 2 Data flow chart for parallelizing the angles-only track-initiation method

of the element space. This means that each combination has to be processed serially. For example, if there are 1,000 new observations at unique time steps, there are up to 166 million combinations to test (1,000-choose-3 combinations). Forming these millions of combinations is prohibitive. Our approach using element partitions and range hypotheses reduces the complexity to N_z^2 in the number of observations. With only two line-of-sight observations required to generate candidate orbits, there are only 500,000 serial combinations to test. However, this approach can be parallelized on two different levels, with respect to element partitions and pairs of observations, potentially allowing high computational throughput in the track-initiation phase of the surveillance problem.

Parallelization is implemented by processing orbital element partitions on different nodes. Either the range–range admissible region described in Sect. 3, or a surveillance region of interest, can be partitioned in this manner. A note on implementation: the partitions can be evenly spaced to cover the search space, or a finer spacing can be used for regions where there is a higher concentration of known objects and sparser spacing used in less populated regions of space. Jones et al. (2015) provides a plot that highlights the uneven distribution of objects in orbit. With this scheme, the partitioning can be adapted to the number of computational cores available. On each core, the combinations of the received observations are checked serially, but only within the partition of orbital elements. Figure 2 highlights the procedure for parallelizing the candidate orbit generation. A major component of this methodology is the ability to limit the range pairs before processing with a Lambert solver by identifying *a priori* what range pairs are feasible within a partition.

The following sections present the range–range admissible region associated with an element partition, together with the range–range hypothesis space that we use to approximate it. We introduce a number of constraint checks that can be performed to identify, with minimal computation, which range hypothesis pairs produce candidate orbits within a partition.

3 Range–range admissible region

This work is focused on estimating the orbits of a large set of new objects, e.g., space debris, in orbit about the Earth. This is a different focus than that of Milani et al. (2004), which estimated the trajectory of an asteroid in a heliocentric orbit. Tommei et al. (2007) first applied the admissible-region method to Earth orbiting objects. The definition of the range–range admissible region adopted here is similar to that presented by Maruskin et al. (2009). Specifically three restrictions are considered: the specific energy must be negative ($E < 0$), the perigee radius of the orbit must not impact Earth ($r_p > R_\oplus + 100\ km$), and the apogee radius must not be too large ($r_a < 25R_\oplus$), where $R_\oplus = 1$ Earth radius. Two examples, representing different orbital regimes (a LEO and GEO), are provided to illustrate the range–range admissible region. A GEO tracking example is the ideal scenario

Table 3 Observer locations $\bar{R}$ and the line-of-sight unit vectors $\bar{u}$ at t_1 and t_2 for the two example scenarios

Parameter	LEO values	GEO values
$\bar{R}_1$	[−5543.8; −2054.6; 2387.8] km	[−5543.8; −2054.6; 2387.8] km
$\bar{R}_2$	[−5505.5; −2155.3; 2387.8] km	[5584.9; 1940.1; 2387.8] km
$\bar{u}_1$	[−0.827; −0.231; 0.513]	[−0.989; −0.1297; −0.0705]
$\bar{u}_2$	[−0.327; −0.914; 0.240]	[0.991; 0.1225; −0.0609]
Δt_{TOF}	250 s	42800 s

The time-of-flight Δt_{TOF} is the difference between the measurement times

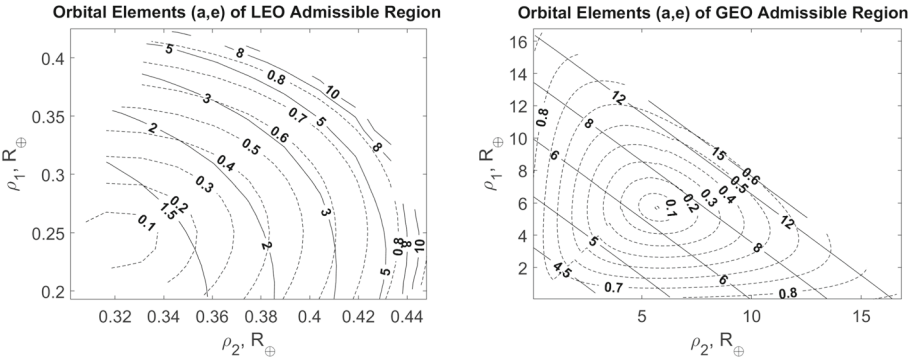

Fig. 3 Examples of range–range admissible regions, a LEO case on the left and a GEO case on the right. Vertical axes represent range hypotheses ρ_1 for observation 1. Horizontal axes represents range hypotheses ρ_2 for observation 2. Both are displayed in units of Earth radii $R_\oplus$. Solid contours are semi-major axis in units of Earth radii. Dashed contours are eccentricity

for the method proposed. The LEO example is included as a contrasting case, to highlight the constraint topography. Table 3 provides the observer locations and line-of-sight vectors for the examples. Figure 3 shows the two examples of the range–range admissible region in terms of eccentricity and semi-major axis contours. For example, if the analyst expects to observe a circular orbit, these plots indicate what range values could possibly define such an orbit. While much work in the literature has been devoted to studying the admissible region and its evolution in terms of range and range rate, here we are interested in range–range constrained regions based on partitioning the search space in order to improve parallelization.

4 Range–range constrained admissible region

Maximizing the performance in the parallelized environment requires efficient constraints based on a logical taxonomy. The space domain is typically described by the altitude of the orbit, or unique values of eccentricity and inclination, guiding our choice to use orbital elements for the partitions. The following constraints have been identified to partition the space domain based on Keplerian orbital elements, focusing on three elements: semi-major axis a, eccentricity e, and inclination i. A partition is specified with subscripts of the minimum and maximum values: $[a_{\min}, a_{\max}]_j$, applicable to partition j, which will of course have bounds on e and i as well. When an element is an unknown in an equation it is specified with an asterisk superscript: a^*. Some of the constraints can be posed directly in terms of the

hypothesized range ρ, and some are more suitably posed in terms of the position vectors: $\bar{r}$. The position vector can be defined with the observer position $\bar{R}$ and the observed line-of-sight $\bar{u}$:

$$\bar{r} = \bar{R} + \rho\bar{u}. \tag{1}$$

The given time-of-flight (TOF) is $\Delta t_{\text{TOF}} = t_2 - t_1$. The angle between the two observed positions $\bar{r}_1 = \bar{r}(t_1)$ and $\bar{r}_2 = \bar{r}(t_1)$ is the change in true anomaly, $\Delta\nu$. Magnitudes of the position vectors are shown without an overbar: $r = \|\bar{r}\|$. Some useful identities in the derivation and definition of the constraints are the chord c and semi-perimeter s:

$$c = \|\bar{r}_2 - \bar{r}_1\| \tag{2}$$

$$s = \frac{1}{2}(r_1 + r_2 + c). \tag{3}$$

The first subsection outlines the starting point of the process: to find the most conservative set of bounds on (ρ_1, ρ_2). While convenient in mitigating the need to consider infinite values of ρ, the supremum bounds do not sufficiently reduce the set of range hypotheses to the RR-CAR as desired. It requires several constraints to do so. Some constraints are particularly effective at rejecting hypothesis pairs defining orbits outside of the partitions, specifically the constraints described in Sects. 4.5 and 4.6. For completeness, all the constraints we have identified are presented. Depending on the approach undertaken, if a range pair hypothesis is rejected due to any of the constraints, it can be removed from consideration. Alternatively, if the range hypotheses are processed as a batch, the intersection of all the constraints is used.

4.1 Supremum bounds on range

Assuming that all orbits of interest are elliptical, will constrain the orbital radii to lie between the smallest allowable perigee and the largest allowable apogee:

$$a_{\min}(1 - e_{\max}) \leq r \leq a_{\max}(1 + e_{\max}). \tag{4}$$

The values of range that correspond to these limits on orbital radius can be found explicitly using the vector triangle relationship of Eq. 1. Considering the perigee case and squaring:

$$a_{\min}^2(1 - e_{\max})^2 \leq \bar{R} \cdot \bar{R} + 2(\bar{R} \cdot \bar{u})\rho + \rho^2. \tag{5}$$

Rearranging the equation leads to a quadratic equation in terms of ρ:

$$\rho^2 + 2(\bar{R} \cdot \bar{u})\rho - [a_{\min}^2(1 - e_{\max})^2 - \bar{R} \cdot \bar{R}] \geq 0. \tag{6}$$

The roots of this equation provide a lower limit on range based on the smallest allowable perigee. Negative roots can be ignored because the range values must be non-negative. The lower supremum bound is:

$$\rho \geq -(\bar{R} \cdot \bar{u}) + \sqrt{(\bar{R} \cdot \bar{u})^2 + a_{\min}^2(1 - e_{\max})^2 - \bar{R} \cdot \bar{R}}. \tag{7}$$

Similarly, for the largest possible apogee, the upper limit on range is:

$$\rho \leq -(\bar{R} \cdot \bar{u}) + \sqrt{(\bar{R} \cdot \bar{u})^2 + a_{\max}^2(1 + e_{\max})^2 - \bar{R} \cdot \bar{R}}. \tag{8}$$

The supremum bounds on range are useful as a first step to limit the hypotheses under consideration. They are especially attractive because they are explicit bounds on range that can be computed for each line-of-sight vector individually. However, there will still be a large

set of hypotheses that are not valid within the partitions on a and e, and the inclination is not taken into account at all. Consequently, additional constraints are needed to improve the efficiency of rejecting range hypotheses. The rest of the constraints presented in the following subsections depend on a pair of range hypotheses.

4.2 Inclination

The orientation of the orbit can be partitioned based on the inclination using the interval $[i_{\min}, i_{\max}]$. Calculate the unit vector $\bar{n}$ normal to the candidate orbital plane:

$$\bar{n} = \pm \frac{\bar{r}_1 \times \bar{r}_2}{\|\bar{r}_1 \times \bar{r}_2\|}. \tag{9}$$

The ambiguous sign depends on whether the transfer is a short-way (+) or long-way (−) transfer. With the sign chosen, the inclination is given unambiguously for a range pair by:

$$\cos(i) = \bar{n} \cdot \bar{k}. \tag{10}$$

The inclination of the candidate orbit lies in the specified interval $[i_{\min}, i_{\max}]$ provided that $\cos(i)$ lies in the interval $[\cos(i_{\max}), \cos(i_{\min})]$. Thus the constraint check is:

$$\begin{aligned} &\cos(i_{\max}) \le \bar{n} \cdot \bar{k} \le \cos(i_{\min}), \\ &\text{Reject otherwise.} \end{aligned} \tag{11}$$

In the case of low-inclination intervals, it may be advisable to replace Eq. 11 with:

$$\sin(i_{\min}) \le \sqrt{1 - (\bar{n} \cdot \bar{k})^2} \le \sin(i_{\max}). \tag{12}$$

4.3 Zero-energy time of flight

This work is concerned with tracking objects in orbit around the Earth; hence, hypotheses can be limited to captured orbits. For a given pair of position vectors, the possible TOF values decrease monotonically with orbital energy. Elliptic (negative-energy) orbits will always have a TOF longer than the parabolic case (zero-energy), and hyperbolic (positive-energy) orbits will always have a TOF that is shorter. The TOF for the zero-energy case Δt_{ZE} is the classical parabolic TOF, so the negative-energy constraint becomes:

$$\begin{aligned} &\Delta t_{ZE} = \frac{4}{3}\sqrt{\frac{a_0^3}{\mu}}(1 \pm \lambda^3) \\ &\text{Reject if } \Delta t_{\text{TOF}} \le \Delta t_{ZE}. \end{aligned} \tag{13}$$

The ambiguous sign depends on whether the transfer is a short-way (+) or long-way (−) transfer. See Battin (1999) pp. 276–277 for a development of Euler's equation for parabolic orbits. The parameter λ is defined in terms of the position vectors:

$$\lambda^2 = \frac{r_1 + r_2 - \|\bar{r}_2 - \bar{r}_1\|}{r_1 + r_2 + \|\bar{r}_2 - \bar{r}_1\|}. \tag{14}$$

4.4 Special Lambert solutions

The geometry of an ellipse leads to some useful restrictions which are considered special solutions of Lambert's problem. For a given pair of positions $\bar{r}_1$ and $\bar{r}_2$ there is a lower limit on the eccentricity that is realizable. Call this value e_0. Battin (1999) discusses the fundamental ellipse on p. 256, calling e_0 the minimum eccentricity of all possible orbits connecting $\bar{r}_1$ and $\bar{r}_2$. That is, the geometry of $\bar{r}_1$ and $\bar{r}_2$ is guaranteed to have an eccentricity greater than e_0. Therefore if e_0 is larger than the upper partition value of eccentricity, that particular range hypothesis pair can be rejected.

$$e_0 = \frac{|r_1 - r_2|}{\|\bar{r}_2 - \bar{r}_1\|}, \quad \text{Reject if } e_0 > e_{\max}. \tag{15}$$

Likewise there is a lower limit on the possible semi-major axis value, a_0. Battin (1999) presents a_0 for the minimum-energy orbit on p. 240. If a_0 is larger than the partition bounds on semi-major axis reject that range pair hypothesis:

$$a_0 = \frac{1}{4}(r_1 + r_2 + \|\bar{r}_2 - \bar{r}_1\|) = \frac{1}{2}s, \quad \text{Reject if } a_0 > a_{\max}. \tag{16}$$

Refer to Chapter 6 of Battin (1999) for an in-depth discussion of the geometry of the orbital problem, and visualizations of the minimum possible elements. While useful, these constraints are limited in utility because they bound the hypothesis region with only lower limits. The following two constraints are important contributions because they bound the hypothesis region with lower and *upper* limits.

4.5 Vacant focus geometry

The RR-CAR can be bounded with the lower and upper limits of the eccentricity partition by considering the geometry of the locus of vacant foci. Battin (1999) discusses the geometry of this locus in detail. The vacant focus must lie along a hyperbola between the two position locations. Specifying bounds on eccentricity $[e_{\min}, e_{\max}]$ limits how close or far the vacant focus can lie from the primary focus or central body. Assuming Keplerian motion and solving for the position of the vacant focus relative to the primary focus leads to the following constraint equation:

$$e_{\min}^2 \leq \frac{c^2 f(p^*)}{\|\bar{r}_1 \times \bar{r}_2\|^2} \leq e_{\max}^2. \tag{17}$$

The full derivation is provided in "Appendix A". To simplify the derivation and discussion, the variable $f(p^*)$ is introduced, a quadratic function of the semi-latus rectum p^*:

$$f(p^*) = p^{*2} - (1 - e_0^2)(r_2 + r_1)p^* + r_1 r_2 (1 - e_0^2). \tag{18}$$

The extremes of Eq. 18, $[f(\cdot)_{\min}, f(\cdot)_{\max}]$, must be tested in Eq. 17, therefore requiring the extremes of p^*:

$$\begin{aligned} p_{\min} &= a_{\min}(1 - e_{\max}^2) \\ p_{\max} &= a_{\max}(1 - e_{\min}^2). \end{aligned} \tag{19}$$

The quadratic $f(p^*)$ is concave up with a minimum value at p_{fmin}. It is not immediately clear from Eq. 18 which side of the minimum value the semi-latus rectum partition

$[p_{\min}, p_{\max}]$ is on. The simplest way to handle the issue is to use the minimum and maximum functions:

$$\begin{aligned} f(p^*)_{\min} &= \min(f(p_{\min}), f(p_{\max})) \\ f(p^*)_{\max} &= \max(f(p_{\min}), f(p_{\max})). \end{aligned} \tag{20}$$

Alternatively, a logic check can be performed to find which side of the minimum value $p_{f_{\min}}$ that $[p_{\min}, p_{\max}]$ lies on. Taking the derivative of $f(p^*)$ and solving for the minimum:

$$p_{f_{\min}} = \frac{1}{2}(1 - e_0^2)(r_2 + r_1). \tag{21}$$

A special check is required in case the partition straddles the minimum. When $p_{\min} < p_{f_{\min}} < p_{\max}$, the lower extreme of $f(p^*)$ must be replaced with $f(\cdot)_{\min} = f(p_{f_{\min}})$. Using the extremes of $f(p)$, the constraint takes the form:

$$\begin{aligned} &e_{\min}^2 \leq \frac{c^2 f(\cdot)_{\max}}{\|\bar{r}_1 \times \bar{r}_2\|^2} \quad \text{and} \quad \frac{c^2 f(\cdot)_{\min}}{\|\bar{r}_1 \times \bar{r}_2\|^2} \leq e_{\max}^2, \\ &\text{Reject otherwise.} \end{aligned} \tag{22}$$

Note that there may be situations where e_0, the smallest possible eccentricity allowable given the geometry, is larger than $e_{\max}$. In these situations it is assumed that the hypothesis has already been rejected per Eq. 15.

4.6 Monotonic time of flight

Since the TOF varies monotonically with the semi-major axis (orbital energy) the range hypotheses can similarly be bounded with lower and upper limits through the semi-major axis partition $[a_{\min}, a_{\max}]$. The semi-major axis partition must be transformed into a partition on TOF, $[\Delta t_{\min}, \Delta t_{\max}]$. Lagrange's form of Kepler's equation provides a means to do so (Battin 1999, p. 278):

$$\Delta t(a^*, \bar{r}_1, \bar{r}_2) = \sqrt{\frac{a^{*3}}{\mu}}\big(\alpha - \beta - (\sin\alpha - \sin\beta)\big). \tag{23}$$

Here is where our discussion is limited to the case of one revolution in the Lambert solution. Augmenting Eq. 23 to allow multiple-revolution solutions presents no essential difficulty. The bookkeeping for hypothesis management has to accommodate possible multiple Lambert solutions per range pair hypothesis. However, the overall constraint logic proposed here for rejecting hypotheses is not changed. The angles α and β in Eq. 23 are defined as:

$$\begin{aligned} \sin\frac{\alpha}{2} &= \sqrt{\frac{s}{2a^*}} \\ \sin\frac{\beta}{2} &= \sqrt{\frac{s-c}{2a^*}}. \end{aligned} \tag{24}$$

This version of the TOF equation is a function of the unknown semi-major axis a^* and the range hypotheses through c and s which are defined in Eqs. 2 and 3, respectively. Care must be taken with the quadrant ambiguities:

Table 4 Orbital partitions for constraint examples

Parameter	LEO	GEO
a (km)	[7478.1 8278.1]	[41164 43164]
e	[0 0.15]	[0 0.04]
i (°)	[15 35]	[0 5]

$$\begin{aligned} &\text{If } \Delta t_{\text{TOF}} > \Delta t(a_0, \bar{r}_1, \bar{r}_2), \\ &\text{Then } \alpha = 2\pi - \alpha_0; \end{aligned} \tag{25}$$

$$\begin{aligned} &\text{If } \Delta\nu > \pi, \\ &\text{Then } \beta = -\beta_0. \end{aligned} \tag{26}$$

Here the terms α_0 and β_0 are the principal values from the equations in Eq. 24. In Eq. 25, the term $\Delta t(a_0, \bar{r}_1, \bar{r}_2)$ is the TOF of the minimum-energy ellipse, which can be found using the minimum possible semi-major axis a_0 from Eq. 16. Prussing (1979) provides a short and enlightening discussion of the geometric interpretation of α and β. Note that there will be a different TOF partition for each pair of range hypotheses, or for each Lambert solution, if multiple revolutions are allowed. Once the TOF partitions are computed, a range pair hypothesis can be checked to see if it is consistent with the given TOF (Δt_{TOF}):

$$\begin{aligned} &\Delta t_{\min} \leq \Delta t_{\text{TOF}} \leq \Delta t_{\max}, \\ &\text{Reject otherwise.} \end{aligned} \tag{27}$$

5 Numerical examples

Two examples are provided to illustrate the constraints presented. These examples are a continuation of those presented in Sect. 3. These examples were arbitrarily chosen to highlight the difference in constraint topography for two common orbits: LEO and GEO. The orbital element partitions for both cases are provided in Table 4.

As discussed in Sect. 4.1, the supremum bounds are found first and set as the axis limits of the plots in this section. This is step 3 of Table 2. After identification of the supremum bounds on range, an evenly spaced grid of hypothetical range values is created for the two line of sights, i.e., step 4. The grid is arbitrarily chosen to be 500×500 samples. Hence, there are 250,000 range pairs created and checked. Step 5 of Table 2 involves testing the range pair hypotheses with each of the constraints from Sect. 4. In the following plots each of the constraints are plotted separately; then, they are combined to show how well the hypothesis region bounds the actual RR-CAR found via a full search with Lambert's method. Red regions are rejected range pairs, and the blue regions are accepted range pairs. In the total constraint plot, the green region is the actual RR-CAR.

The goal of developing constraints was to efficiently reject cases outside of the given partition. Hence, if the blue region were significantly larger than the green region, then the constraints would be inefficient. Conversely if the blue region were smaller than the green region, then valid cases would be rejected causing the method to miss candidate orbits. Ideally the blue hypothesis region just barely overlaps the green RR-CAR.

Figure 4 shows the LEO example. The observer positions and LOS vectors are provided in Table 3. The top row of plots on the left of Fig. 4 show the effect of the special Lambert solution constraints a_0, e_0, and Δt_{ZE}. Along the bottom row are the inclination, time of flight,

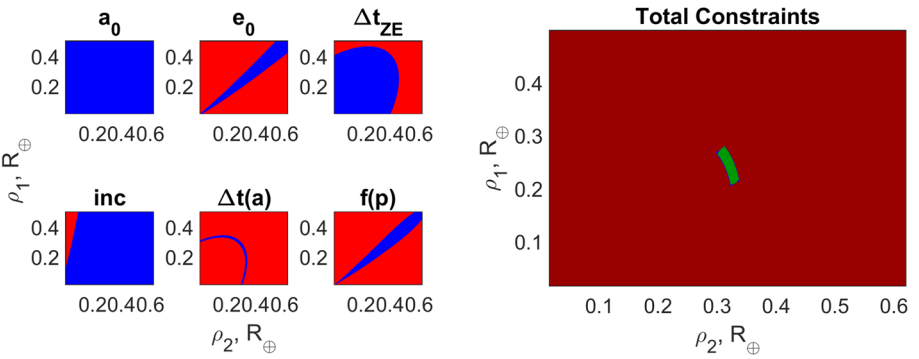

Fig. 4 LEO example showing constraint violations. On the left is each individual constraint shown separately. On the right is the total set of constraints with the RR-CAR shown. Blue is valid hypotheses, red is rejected hypotheses, and green is the RR-CAR

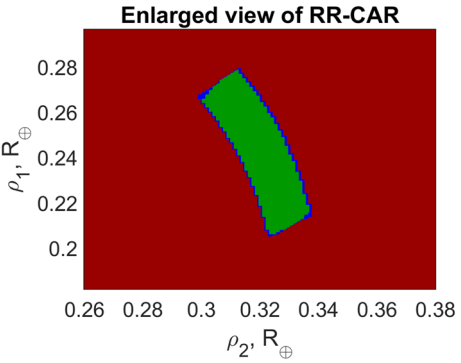

Fig. 5 Enlarged view of the total set of constraints for LEO example. Blue are valid hypotheses, red are rejected hypotheses, and green is the RR-CAR

and vacant focus constraints. On the right of the figure is the union of all the constraints. Of the 250,000 generated samples, only 1,035 pairs pass the constraints, or 0.41% of the total samples. Of those, only 15 samples pass the constraints but are not in the CAR (green region). This is the blue region barely surrounding the CAR. The inefficiency of the constraints is 1.47% (15 of 1,035). At the scale of these plots, it is difficult to see any blue regions since the constraints bound the RR-CAR very well. Figure 5 shows a zoomed in view of the RR-CAR to highlight how effective the constraints are.

The vacant focus constraint is mainly a function of eccentricity and it is comparable to the e_0 constraint. For this case, the a_0 constraint is not active; we have noticed that typically it becomes active for transfer angles near $\Delta\nu \approx 180°$. The time-of-flight constraint eliminates most of the search space, and appears to obviate the need for the zero-energy transfer time constraint.

The GEO example is shown in Fig. 6. This case has a transfer time near $\Delta\nu \approx 180°$, hence the a_0 constraint is active. This geometry also causes the RR-CAR to be fairly large. Here 29,890 pairs pass the constraints, or 11.96%. Of those 236 were not in the CAR, representing only a 0.80% inefficiency. We have noticed that the inclination constraint is almost always active for this example when $\Delta\nu \approx 180°$. Again the hypothesis region bounds the RR-CAR closely.

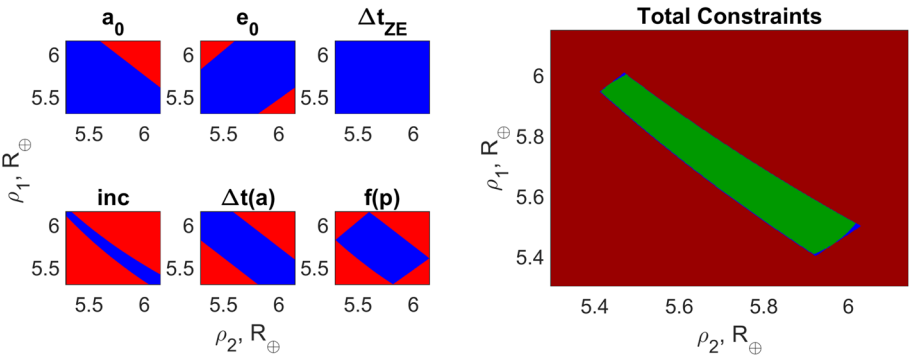

Fig. 6 GEO example showing constraint violations. On the left is each individual constraint shown separately. On the right is the total set of constraints with the RR-CAR shown. Blue are valid hypotheses, red are rejected hypotheses, and green is the RR-CAR

6 Discussion

Although every orbit within the element-space partition corresponds to values of range that lie within the bounds given here, some values of range that satisfy the bounds may lead to orbits that lie outside the given partition. This circumstance represents inefficiency in the parallelization of track initiation: nearly the same candidate orbits near the boundaries of the element-space partitions may be generated in both of the adjacent partitions, if the range hypotheses are planted densely enough. Using small partitions with dense grids could also allow the use of linearized Lambert solutions as presented by McMahon and Scheeres (2016) to further reduce the computational burden. How to sample the hypothesis regions is, in fact, still an open question for hypothesis methods such as this. Typical approaches use either a rectangular grid or a Delaunay triangulation (Tommei et al. 2007), but an alternate approach using an iso-energy grid has been suggested by Siminski et al. (Siminski et al. 2013a, b).

In any case, no candidate orbits within the given element-space partitions will be missed because of the bounds and other checks given here. The extent and cost of the inefficient duplication of candidate orbits will depend on the particular data-sets and element partitions of interest, and may require further study if the tracking scenario is computationally stressing. In practice, of course, within any element partition, any of these extra orbit hypotheses can be either kept or discarded. If they are kept, we would have, at most, a bookkeeping problem of transferring the extra orbit solutions to the correct element partition. The trade-off in this case is that merely moving data between processors always takes time. We note also that each candidate orbit is used in exactly the same way, and the overall tracking job proceeds in the same way, regardless of whether any candidate orbits happen to originate in an unintended element partition, as long as all observations are available to each processor.

6.1 Comparison to traditional methods

The approach outlined in this work allows us to make use of an already proven method (the Search and Determine algorithm and software, SAD) that was designed for generating and testing data association hypotheses for position-type observations typical of radar sensors (Coffey et al. 1996a, b, 2002). However, our emphasis on generating candidate orbits with a Lambert-based approach in the angles-only case is not merely a matter of convenience in

extending an existing method such as SAD. Certainly, the bounds on range that we present here could be used in a variety of ways with other angles-based initial orbit determination methods. Both the traditional methods of angles-only orbit determination (Escobal 1965) and modern methods such as those of Gooding (1993, 1997), Karimi and Mortari (2011) and others (Sarnecki 1997) rely on solving for the range by either root-finding or optimization. Such algorithms can always be made to work more reliably when rigorous upper and lower bounds on the unknown quantity are available. However, one encounters at least three difficulties in trying to apply direct angles-only methods to a large, multiple-target catalog-building scenario.

First, the direct angles-only methods do not scale to large problems as well as a Lambert-based method does. Of course, it may not be clear a priori in any particular case which approach finally requires fewer processors to achieve a desired production rate of orbit solutions. Higher-degree polynomial scaling requires more processors with traditional approaches and smaller element partitions require more processors on the range hypothesis approach. The choice may depend on the size and character of the data-set itself and the element partitions of interest.

Second, a Lambert-based method, ideally implemented, will produce a candidate orbit for every real object that has been observed at least twice. In comparison, a direct angles-based method, such as Gooding's, will produce candidate orbits only for those real objects that have been observed at least 3 times. An N_z^4 method will produce candidate orbits only for those real objects that have been observed at least 4 times, and so on. Hence, the Lambert-based method may do a more complete job of generating viable candidate orbits from real data-sets, while scaling more favorably than the direct angles-based methods for large numbers of observations.

Third, although the range bounds presented here allow one to reject candidate solutions based on range, with a direct angles-only method one still has to compute the range in terms of the observations in order to find out if it satisfies the bounds. This turns out to be most of the computation needed to produce the candidate orbits themselves. In the Lambert-based approach, the range bounds allow us to avoid most of the potential computation for the candidate orbits.

6.2 Comparison to angle-rate methods

The use of angle rates, when they are available, is especially important, and has been documented in many papers on the use of the attributable vector (of measured angles and angle rates) originally proposed by Milani et al. (2004). If angle rates are available or can be derived from the observation data, a complete orbit hypothesis can be formed for each observation without any iterative solutions, merely by choosing a value of range and a value of range rate. This is the approach outlined by DeMars et al. (2010, 2012), where the use of an element-space partition via the constrained admissible region in the range–range-rate plane is first introduced. For example, denoting the gravitational parameter by μ, write the first integrals of Keplerian motion as:

$$\text{Energy:} \quad E = (\dot{\bar{r}} \cdot \dot{\bar{r}})/2 - \mu/\|\bar{r}\| \tag{28}$$

$$\text{Angular momentum:} \quad \bar{h} = \bar{r} \times \dot{\bar{r}} \tag{29}$$

$$\text{Laplace vector:} \quad \mu\bar{e} = \dot{\bar{r}} \times (\bar{r} \times \dot{\bar{r}}) - \mu\bar{r})/\|\bar{r}\|. \tag{30}$$

Given the vector triangle relation $\bar{r} = \bar{R} + \rho\bar{u}$ and its time derivative for each observation, the CAR can be defined in the $(\rho, \dot{\rho})$ plane for each partition in the space of elements by means of inequalities such as:

$$-\mu/(2a_{\min}) \leq E \leq -\mu/(2a_{\max}) \tag{31}$$

$$\cos i_{\max} \leq (\bar{h}/\|\bar{h}\|) \cdot \bar{k} \leq \cos i_{\min} \tag{32}$$

$$e_{\min} \leq \|\bar{e}\| \leq e_{\max}. \tag{33}$$

Here $\bar{k}$ is the north polar unit vector in the Earth-centered inertial frame. For each observation, the values of range and range rate that satisfy these inequalities will result in orbits that lie only within the given partition of the space of elements. As in the angles-only case, this track-initiation problem is parallel with respect to element partitions. If provided with bounds on range and range rate for each element partition, the number of orbit hypotheses needed can be reduced for each partition by making the partitions smaller and using more processors to cover the whole element space. DeMars and Jah (2012) have shown what the CAR looks like for partitions of semi-major axis and eccentricity by a numerical treatment of the above inequalities. Maruskin et al. (2009) have shown how the admissible regions evolve in time and how the overlap of the admissible regions for different observations can help solve the data association problem.

With accurate angle rates the track-initiation job scales linearly with the number of observations rather than as the square or cube, with a computational load proportional to $(N_z N_\rho N_{\dot{\rho}})$ if $N_{\dot{\rho}}$ is the number of range rate hypotheses assigned to each observation. One could hardly expect to do any better than this in solving a large track-initiation problem using optical data. Our concern is with the case when usable angle rates are not available, as when we have widely separated angles-only observations. The usual attributable-vector and admissible-region analysis leads nowhere if angle rates are not available. For example, the track-initiation method of DeMars et al. (2010), involving multiple hypotheses on range and range rate, requires simultaneous angle and angle-rate values. Similarly, the correlation and orbit determination study performed by Milani et al. (2011), which used an admissible-region analysis, used simultaneous angle and angle-rate data. At present only direct angles-only methods that solve for the ranges are available to handle the angles-only track-initiation problem. In this analysis we have offered a Lambert-based alternative that may scale better with respect to the number of observations than any current angles-only method.

6.3 Future work

Several approximations were made to develop this methodology which will need to be addressed in future studies. For instance, Keplerian orbital dynamics is assumed in this work. Optical observations are typically the main source of data for objects in higher orbits, where the effects of drag are minimal, allowing simple dynamics approximation to hold for longer periods. Further the time between observations of the same object will often be short considering the amount of data generated by modern sensors. Hence it is assumed that the impact of using simplified dynamics will be minimal. Future work should address the robustness of the method when incorporating higher fidelity dynamics.

Another concern ignored in this article is the robustness of the method to noisy observations. Considering the effectiveness of the constraints it is feasible that some range pair hypotheses may be rejected erroneously due to measurement uncertainty. If range hypotheses are densely chosen (with a fine grad spacing), then it is likely that hypotheses along the constraint boundaries will be close enough together to still generate an acceptable candidate

target. This effect could be further remedied by padding the constraint tolerances. Roscoe et al. (2014) investigated some of the effects of angle-rate measurement noise; a similar study of typical uncertainty for angles-only observations should be investigated.

7 Conclusions

In this paper, a method is proposed to generate candidate orbits from a large data-set of uncorrelated angles-only observations. The method takes advantage of modern day supercomputers with the ability to process in parallel on hundreds or thousands of nodes. Parallelization is made possible by partitioning the search space, the range–range admissible region or the surveillance region of the sensor, via the orbital elements: a, e, i.

The static constraint checks developed in this article are applied to efficiently retain only physically feasible range pairs in the search space. A Lambert solver is then used to compute candidate orbits based on this reduced set of range pairs. Because a Lambert solver is an iterative method, the use of our constraints reduces the overall computational burden. Examples are provided to highlight the range–range admissible region and to demonstrate the various constraints developed. The efficiency of the constraints for two examples is around 98–99% with zero false rejections.

Now that the foundation is laid, future efforts will explore performance comparisons with existing methods. It is our hope that this work will have direct impact on the ability of an operational tracking system to respond quickly to future break-up events.

Funding John Gaebler performed a portion of this work during an internship in the AFRL Scholars program. Paul Schumacher's contribution was partially funded by the Air Force Office of Scientific Research under Project Number FA9550-16RDCOR283.

Compliance with ethical standards

Conflict of interest The authors declare that they have no conflict of interest.

Appendix A: Derivation of vacant focus constraint

Assuming Keplerian motion, the derivation is limited to the two-dimensional space of the orbital plane. The vacant focus location (X, Y) relative to the primary focus must reside at the common point of three circles. One circle is around the primary focus with a radius of $2a^*e^*$, where a^* and e^* are the unknown semi-major axis and eccentricity. This circle represents the distance the vacant focus can be from the primary. Two more circles are defined around $\bar{r}_1$ and $\bar{r}_2$ with radii $q_1 = 2a^* - r_1$ and $q_2 = 2a^* - r_2$, respectively. See Fig. 7 for a visualization of the circles defined here.

The system of equations for the three circles is:

$$(X)^2 + (Y)^2 = (2a^*e^*)^2 \tag{34}$$

$$(X - r_{1x})^2 + (Y - r_{1y})^2 = (2a^* - r_1)^2 \tag{35}$$

$$(X - r_{2x})^2 + (Y - r_{2y})^2 = (2a^* - r_2)^2. \tag{36}$$

In expanded form Eqs. 35 and 36 are:

$$X^2 + Y^2 - 2r_{1x}X - 2r_{1y}Y = 4a^{*2} - 4r_1a^* \tag{37}$$

$$X^2 + Y^2 - 2r_{2x}X - 2r_{2y}Y = 4a^{*2} - 4r_2a^*. \tag{38}$$

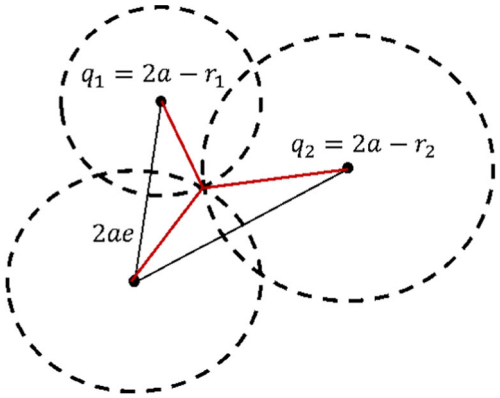

Fig. 7 Geometry used to find the location of the vacant focus relative to the primary focus (lower left point). Equations in the figure define the length of the radius (red line) for each circle

Substituting Eq. 34 into Eqs. 37 and 38 while also introducing the semi-latus rectum p^* gives:

$$r_{1x}X + r_{1y}Y - 2r_1a^* = -2a^*p^* \tag{39}$$
$$r_{2x}X + r_{2y}Y - 2r_2a^* = -2a^*p^*. \tag{40}$$

The desired location of the vacant focus (X, Y) relative to the central body can be obtained after some algebra:

$$X = \frac{2a^*p^*(r_{1y} - r_{2y}) + 2a^*(r_1r_{2y} - r_2r_{1y})}{r_1r_2\sin\Delta\nu} \tag{41}$$
$$Y = \frac{2a^*p^*(r_{1x} - r_{2x}) + 2a^*(r_1r_{2x} - r_2r_{1x})}{r_1r_2\sin\Delta\nu}, \tag{42}$$

where $\Delta\nu$ is the angular separation between the two observations. Replace X and Y in Eq. 34, perform several steps of algebra, and the equation becomes:

$$\frac{p^{*2}\|\bar{r}_2 - \bar{r}_1\|^2 + 2p^*r_1r_2(\cos\Delta\nu - 1)(r_2 + r_1) + 2r_1^2r_2^2(1 - \cos\Delta\nu)}{r_1^2r_2^2\sin^2\Delta\nu} = e^{*2}. \tag{43}$$

Introducing some useful identities

$$c^2 = \|\bar{r}_2 - \bar{r}_1\|^2 \tag{44}$$
$$r_2^2 + r_1^2 - c^2 = 2r_1r_2\cos\Delta\nu \tag{45}$$
$$e_0^2 = \frac{(r_1 - r_2)^2}{c^2} \tag{46}$$
$$\|\bar{r}_1 \times \bar{r}_2\|^2 = r_1^2r_2^2\sin^2\Delta\nu, \tag{47}$$

leads to:

$$\frac{c^2(p^{*2} + (1 - e_0^2)(r_2 + r_1)p^* + r_1r_2(1 - e_0^2))}{\|\bar{r}_1 \times \bar{r}_2\|^2} = e^{*2}. \tag{48}$$

At this point it is convenient to specify a function $f(\cdot)$ as:

$$f(p^*) = p^{*2} - (1 - e_0^2)(r_2 + r_1)p^* + r_1r_2(1 - e_0^2), \tag{49}$$

giving a compact equation:

$$\frac{c^2 f(p^*)}{\|\bar{r}_1 \times \bar{r}_2\|^2} = e^{*2}. \tag{50}$$

An analysis to verify that the function defined in Eq. 49 will always be bounded is required. Descartes rule of signs tell us that $f(p^*)$ will always have two positive real roots, or no real roots, and will be concave up. Rearranging Eq. 50:

$$f(p^*) = \frac{e^{*2}\|\bar{r}_1 \times \bar{r}_2\|^2}{c^2}. \tag{51}$$

Since all the factors on the right hand side of Eq. 51 must be positive, then $f(p^*) \geq 0$, and there can be no real roots. Returning to Eq. 50 and introducing the orbital element partitions on eccentricity, the desired constraint equation arises:

$$e^2_{\text{min}} \leq \frac{c^2 f(p^*)}{\|\bar{r}_1 \times \bar{r}_2\|^2} \leq e^2_{\text{max}}. \tag{52}$$

To check this constraint, the extremes of p^* are used to find the respective extremes of $f(p^*)$. It is important to note that if the extremes on p^* bound the minimum of the function $f(p^*)$, then the smallest possible value will be $f(p_{\text{fmin}})$. The minimum value of $f(p^*)$ is given by:

$$\frac{\partial f(p^*)}{\partial p^*} = 2p^* - (1 - e_0^2)(r_2 + r_1) \tag{53}$$

$$0 = 2p_{\text{fmin}} - (1 - e_0^2)(r_2 + r_1) \tag{54}$$

$$p_{\text{fmin}} = \frac{1}{2}(1 - e_0^2)(r_2 + r_1). \tag{55}$$

References

Battin, R.: An Introduction to the Mathematics and Methods of Astrodynamics, pp. 237–294. AIAA, Reston (1999)

Coffey, S., Healy, L., Neal, H.: Applications of parallel processing to astrodynamics. Celest. Mech. Dyn. Astron. **66**(1), 61–70 (1996a)

Coffey, S., Jenkins, E., Neal, H., Reynolds, H.: Parallel processing of uncorrelated observations into satellite orbits. In: Proceedings of the 6th AAS/AIAA Space Flight Mechanics Conference, Advances in the Astronautical Sciences, Austin, Texas (1996b)

Coffey, S., Neal, H., Berry, M.: Uncorrelated observations processing at naval space command. J. Guid. Control Dyn. **25**, 676–684 (2002)

DeMars, K., Jah, M.: Initial orbit determination via Gaussian mixture approximation of the admissible region. In: Proceedings of the 22nd AAS/AIAA Space Flight Mechanics Conference, Advances in the Astronautical Sciences, Charleston, South Carolina, vol. 143 (2012)

DeMars, K., Jah, M., Schumacher Jr, P.: The use of angle and angle rate data for deep-space orbit determination and track association. In: Proceedings of the 20th AAS/AIAA Space Flight Mechanics Conference, Advances in the Astronautical Sciences, San Diego, California, vol. 136 (2010)

DeMars, K., Jah, M., Schumacher Jr., P.: Initial orbit determination using short-arc angle and angle rate data. IEEE Trans. Aerosp. Electron. Syst. **43**(3), 2628–2637 (2012)

Escobal, P.: Methods of Orbit Determination. Wiley, reprint with corrections by Krieger Publishing Company, 1976 (1965)

Farnocchia, D., Tommei, G., Milani, A., Rossi, A.: Innovative methods of correlation and orbit determination for space debris. Celest. Mech. Dyn. Astron. **107**, 169–185 (2010)

Fujimoto, K., Alfriend, K.T.: Optical short-arc association hypothesis gating via angle-rate information. J. Guid. Control Dyn. **38**(9), 1602–1613 (2015)

Fujimoto, K., Maruskin, J., Scheeres, D.: Circular and zero-inclination solutions for optical observations of earth-orbiting objects. Celest. Mech. Dyn. Astron. **106**, 157–182 (2010)
Gaebler, J., Axelrad, P., Schumacher Jr, P.: Boundaries on range–range constrained admissible regions for optical space surveillance. In: Advanced Maui Optical and Space Surveillance Technologies Conference (AMOS) (2017)
Gooding, R.: A new procedure for orbit determination based on three lines of sight (angles only). Tech. rep., Defense Research Agency Technical Report 93004, Farnborough, Hampshire, GU14 6TD, United Kingdom, available through Defense Technical Information Center and National Technical Information Service (USA) (1993)
Gooding, R.: A new procedure for the solution of the classical problem of minimal orbit determination from three lines of sight. Celest. Mech. Dyn. Astron. **66**(4), 387–423 (1997)
Gronchi, G., Dimare, L., Milani, A.: Orbit determination with the two-body integrals. Celest. Mech. Dyn. Astron. **107**, 299–318 (2010)
Jones, J., Bryant, D., Vo, B., Vo, B.: Challenges of multi-target tracking for space situational awareness. In: 18th International Conference on Information Fusion, IEEE (2015)
Jones, J., Vo, B., Vo, B.: Generalized labeled multi-Bernoulli space-object tracking with joint prediction and update. In: AIAA/AAS Astrodynamics Specialist Conference (2016)
Karimi, R., Mortari, D.: Initial orbit determination using multiple observations. Celest. Mech. Dyn. Astron. **109**(2), 167–180 (2011)
Maruskin, J., Scheeres, D., Alfriend, K.: Correlation of optical observations of objects in earth orbit. J. Guid. Control Dyn. **32**, 194–209 (2009)
McMahon, J., Scheeres, D.: Linearized Lambert's problem solution. J. Guid. Control Dyn. **39**(10), 2205–2218 (2016)
Milani, A., Knezevic, Z.: From astrometry to celestial mechanics: orbit determination with very short arcs. Celest. Mech. Dyn. Astron. **92**, 1–18 (2005)
Milani, A., Gronchi, G., Vitturi, M., Knezevic, Z.: Orbit determination with very short arcs: I. Admissible regions. Celest. Mech. Dyn. Astron. **90**(1), 57–85 (2004)
Milani, A., Tommei, G., Farnocchia, D., Rossi, A., Schildknecht, T., Jehn, R.: Correlation and orbit determination of space objects based on sparse optical data. Mon. Not. R. Astron. Soc. **417**(3), 2094–2103 (2011)
Prussing, J.E.: Geometrical interpretation of the angles α and β in Lambert's problem. J. Guid. Control Dyn. **2**(5), 442–443 (1979)
Roscoe, C., Schumacher Jr., P., Wilkins, M.: Parallel track initiation for optical space surveillance using range and range-rate bounds. Adv. Astron. Sci. **150**, 989–1008 (2014)
Sarnecki, A.: A projective approach to orbit determination from three sight lines. Celest. Mech. Dyn. Astron. **66**(4), 425–451 (1997)
Schumacher Jr, P.: Bounds on range and range rate for optical tracking of satellites. In: Proceedings of the 9th US-Russian Space Surveillance Workshop, Listvyanka, Russia (2012a)
Schumacher Jr, P., Wilkins, M.: Scalable track initiation for optical space surveillance. In: Proceedings of the Advanced Maui Optical and Space Surveillance Technologies Conference, Wailea, HI (2012b)
Schumacher Jr, P., Wilkins, M., Roscoe, C.: Parallel algorithm for track initiation for optical space surveillance. In: Proceedings of the 6th European Conference on Space Debris, Darmstadt, Germany (2013)
Siminski, J., Montenbruck, O., Fiedler, H., Weigel, M.: Best hypotheses search on iso-energy-grid for initial orbit determination and track association. In: 23rd AAS/AIAA Spaceflight Mechanics Conference, Kauai, Hawaii (2013a)
Siminski, J., Fiedler, H., Schildknecht, T.: Track association performance of the best hypotheses search method. In: Proceedings of the Sixth European Conference on Space Debris, European Space Operations Center, Darmstadt, Germany (2013b)
Siminski, J.A., Montenbruck, O., Fiedler, H., Schildknecht, T.: Short-arc tracklet association for geostationary objects. Adv. Space Res. **53**(8), 1184–1194 (2014)
Tommei, G., Milani, A., Rossi, A.: Orbit determination of space debris: admissible regions. Celest. Mech. Dyn. Astron. **97**, 289–304 (2007)
Tommei, G., Milani, A., Farnocchia, D., Rossi, A.: Correlation of space debris observations by the virtual debris algorithm. In: Proceedings of the Fifth European Conference on Space Debris, European Space Operations Center, Darmstadt, Germany (2009)
Vo, B., Vo, B., Hoang, H.: An efficient implementation of the generalized labeled multi-Bernoulli filter. IEEE Trans. Signal Process. **65**(8), 1975–1987 (2017)